RSC Applied Interfaces

ROYAL SOCIETY OF CHEMISTRY

PAPER

View Article Online
View Journal | View Issue

Cite this: *RSC Appl. Interfaces*, 2026, 3, 527

Facile one-step elaboration of nanostructured $ZnMn_2O_4$ thin films by a plasma process as a high-performance rechargeable zinc-ion battery cathode

Lounis H. Bekkar, [a] Alex Lemarchand, [a] Noël Girodon-Boulandet,[a] Cyrille Bazin, [b] Mathieu Frégnaux, [c] Hubert Perrot [b] and Mehrdad Nikravech *[a]

Received 7th October 2025,
Accepted 7th January 2026

DOI: 10.1039/d5lf00303b

rsc.li/RSCApplInter

The need to develop safe, environmentally-friendly and low cost batteries has led to a growing interest in zinc-ion batteries (ZIBs), due to the abundance of zinc and the high theoretical capacity of this material. For large scale applications, it will be necessary to find adequate cathode materials capable of reversible Zn^{2+} electrochemical storage over prolonged cycling. Among various promising candidates, $ZnMn_2O_4$ spinel has attracted attention because of its high theoretical capacity, higher voltage than vanadium-based cathodes, and better cyclability among manganese oxide-based cathodes. However, most of the elaboration routes of manganese oxide based cathodes rely on cost-ineffective and time-consuming multi-steps processes. In this work, we report the elaboration of nanostructured thin films of $ZnMn_2O_4$ spinel using a single step non-equilibrium plasma method without calcination and without using any additives. The electrochemical behavior of the as-deposited $ZnMn_2O_4$ spinel thin film was studied for application as a cathode in ZIBs. It gave a remarkably high specific capacity of 235 mA h g^{-1} at 0.1 A g^{-1} and 155 mA h g^{-1} after 1100 cycles at a current intensity of 1 A g^{-1}. These electrochemical performance results demonstrate that the plasma-based elaboration process is a promising strategy for the development of advanced next-generation ZIBs based on the use of nanostructured materials with a controlled structure and microstructure.

Introduction

High-performance electric storage devices are considered to be a crucial part of the ongoing clean energy transition.[1] In the upcoming years, the demand for batteries is expected to increase massively in several sectors.[2] One of the key factors explaining the increase in battery demand is the growth of the electric vehicle (EV) market. Indeed, up to 900 million battery-powered electric vehicles are expected globally by 2040.[3] In addition, the storage of renewable energy will be a major driver of battery demand. Renewables are inherently variable and subject to fluctuations. Batteries can help to balance supply and demand, increase the stability of the grid and regulate its frequency. Therefore, they are a real solution to facilitate the integration of renewable energy sources into the grid. Following the "*NET ZERO SCENARIO*",[4] to keep the global temperature increase at +1.5 °C, the installed grid-scale battery storage capacity should expand 44-fold between 2021 and 2030 to 680 GW.

Currently, lithium-ion batteries (LIBs), with organic electrolytes, are the most attractive and widely used energy storage technology.[5,6] Nevertheless, the lack of security, high-cost production, lithium resource limitations and environmental issues are prompting a search for sustainable alternatives to LIBs.[6–8]

In this context, other kinds of rechargeable metal-ion (Na^+,[9] K^+,[10] Mg^{2+},[11] Zn^{2+},[12] Ca^{2+},[13] Al^{3+})[14] batteries with aqueous electrolytes have received extensive attention, as safety, high performance, environmental friendliness, recyclability and low cost are among the required criteria for batteries of the future. Zinc cations present an ionic radius very close to that of lithium. The higher redox voltage of zinc (−0.763 V *vs.* a standard hydrogen electrode (SHE)) allows metallic zinc to be used in slightly acidic aqueous media,[15] and the two-electron transfer mechanism offers zinc a high theoretical specific capacity of 820 mA h g^{-1} or 5854 mA h cm^{-3}. Therefore, zinc-ion batteries (ZIBs) could provide high

[a] *Université Sorbonne Paris Nord, UPR CNRS 3407, Laboratoire des Sciences des Procédés et des Matériaux LSPM, 93430 Villetaneuse, France. E-mail: mehrdad.nikravech@lspm.cnrs.fr*
[b] *Sorbonne Université, UMR CNRS 8235, Laboratoire Interfaces et Systèmes Electrochimiques LISE, 4, place Jussieu, F-75005 Paris, France*
[c] *Institut Lavoisier de Versailles, Université de Versailles Saint-Quentin-en-Yvelines, Université Paris-Saclay, CNRS, UMR 8180, Versailles Cedex 78035, France*

energy density and excellent rate performance.[16,17] Moreover, zinc metal is naturally abundant, evenly spread within the earth's crust, low cost and non-toxic. These attributes make zinc a very promising candidate for producing high-performance aqueous metal-ion batteries.

However, the main challenge that ZIBs are facing is finding adequate cathodic materials capable of reversible Zn^{2+} storage after prolonged cycling.[18] This challenge is even bigger given that the cathode material is arguably one of the most important components in ZIBs, as it influences the overall electrochemical performance of the battery.

So far, three types of cathode materials have been mainly studied for ZIBs: manganese-based oxides,[19] vanadium-based oxides[20] and Prussian Blue analogues.[21] Manganese-based oxides are among the most promising and the most studied ones due to their high capacities and high voltage simultaneously.[22] However, they suffer from capacity decay due to irreversible structural transformations, Mn dissolution, and by-product generation during the charging/discharging process.[23]

It has been reported that the binary manganese oxides have superior rechargeability compared to mono-oxides.[24] Spinel $ZnMn_2O_4$ is one of the binary manganese oxides with a high redox potential, large natural abundance of raw materials and low toxicity to the environment. Inspired by the $LiMn_2O_4$ cathode in LIBs,[25] it has been investigated in many studies as a cathode material for ZIBs.[26–30] Importantly, no phase transition has been observed for this material, leading to stable cycling performance.[24,31]

A wide range of $ZnMn_2O_4$ synthesis routes have been reported to date, including sol–gel,[32,33] solvothermal,[34,35] hydrothermal,[36,37] co-precipitation,[38,39] micro-emulsion[40,41] and solid state methods,[42] as well as microwave-assisted colloidal synthesis,[43] electrospinning[44] and electrodeposition.[24] However, most of the conventional elaboration methods of manganese-based oxides rely on annealing (>400 °C) to achieve sufficient crystallinity and require the incorporation of conductive carbon and polymer binders to ensure electrical conductivity and mechanical stability.[26,31,45–47] These successive steps significantly increase the process complexity, duration, resource consumption and overall manufacturing cost, which limits their suitability for scalable and sustainable electrode production.

In contrast, the present work introduces a one-step route for the elaboration of $ZnMn_2O_4$ spinel cathode materials in the form of nanostructured thin films using a low pressure non-equilibrium plasma process. This approach eliminates the need for high-temperature annealing and avoids any additives, simplifying electrode fabrication while reducing energy input and material use. The resulting $ZnMn_2O_4$ films are directly functional in their as-deposited state, exhibiting a high specific capacity of 235 mA h g^{-1} at 0.1 A g^{-1} and a cyclability of 70% over 2000 cycles at a high current density of 4 A g^{-1}. These performance results highlight the strong potential of the plasma process as an efficient, low-cost and environmentally friendly alternative to conventional synthesis routes. We believe that this work will pave the way for the development of more efficient strategies to obtain high performance battery materials and accelerate the development of next-generation energy technologies, especially in giving fast and cheap ways to meet the exploding battery demand.

Experimental

Deposition of $ZnMn_2O_4$ by the low pressure plasma technique

$ZnMn_2O_4$ thin films were deposited through the plasma technique (Fig. 1a and b). A precursor solution was prepared by dissolving 0.659 g of zinc acetylacetonate hydrate ($Zn(C_5H_7O_2)_2{\cdot}xH_2O$; Sigma-Aldrich) and 1.225 g of manganese acetate ($Mn(C_2H_3O_2)_2{\cdot}4H_2O$; >99.0% Sigma-Aldrich) in 50 mL of anhydrous methanol (CH_3OH; 99.8% Sigma Aldrich) in order to obtain a Zn : Mn molar ratio of 1 : 2 ($[Mn^{2+}]$ = 0.1 M; $[Zn^{2+}]$ = 0.05 M). The precursor solution was nebulized using a home-made ultrasonic sprayer (1 MHz), and then carried into the plasma reactor by a mixture of argon and oxygen gas at a flow rate of 470 mL min^{-1}. There, the droplets are subjected to rapid evaporation as the vapour pressure of the solvent (methanol saturated vapour pressure = 130.2 mbar at 20 °C) is much higher than the 1 to 10 mbar inside the reactor. The plasma chamber is a quartz tube positioned in the centre of an inductive coil and maintained at 60 Pa by a vacuum pump to ensure the consistency and stability of the plasma throughout the deposition process. A radiofrequency power generator coupled with a matchbox provides the plasma discharge at 450 W. The argon and oxygen gas flow rate and plasma discharge power values are, respectively, key parameters to control the residence time of the chemical precursors in the plasma and its reactivity through the amount of reactive species. The influence of these parameters was studied in a previous work[48] and they were fixed here to guarantee the acquisition of a well-crystallized thin film. The substrates used were amorphous quartz, silicon and platinum. The substrate temperature was controlled with a temperature regulation system and maintained between 25 °C and 200 °C. Fig. 1c shows that the samples mass is proportional to the deposition time. The deposition rate was estimated at 20 μg min^{-1} for a 1 cm^2 surface. Considering that 0.6 mg was enough to perform the different characterizations, the deposition time was fixed at 30 min in all experiments.

Structural, microstructural and morphological characterizations

Amorphous quartz was used as a substrate for structural and morphological characterizations. X-ray diffraction (Empyrean Panalytical) using Cu Kα radiation (λ = 1.54 Å) at a scanning 2θ window of 15–70° with a step of 0.05° and a counting time of 44 s was performed. XRD diagrams were treated using the Rietveld method,[49,50] implemented in Fullprof software.[51] Using the Thompson–Cox–Hastings

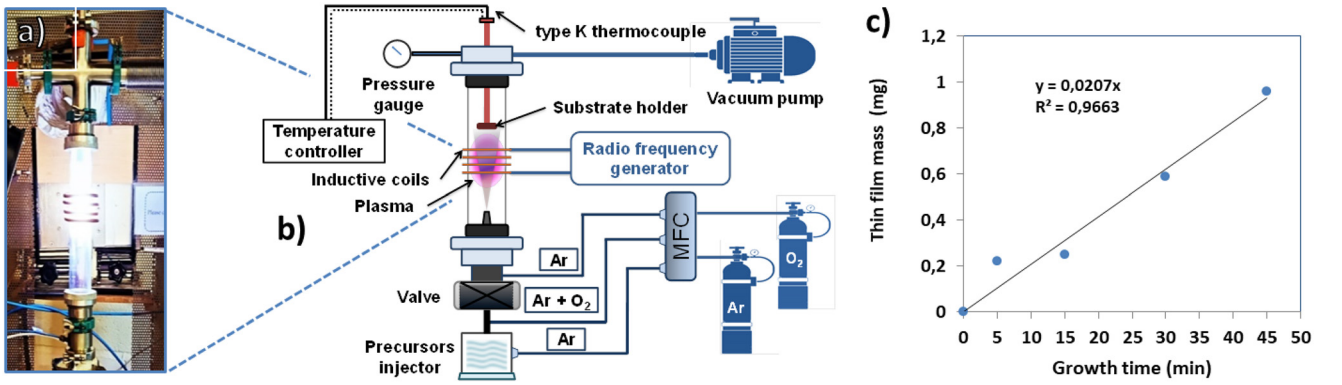

Fig. 1 a) Photograph of the plasma reactor; b) experimental setup; c) low pressure plasma thin film mass as a function of the growth time.

formulation of the pseudo-Voigt line profile function, microstructural information (size, strain) was estimated. Anisotropic particle size was taken into account using the spherical harmonic approach also implemented in the Fullprof software.[52] Morphology was observed by scanning electron microscope (FEG SUPRA 40VP, ZEISS), transmission electron microscope (200 kV JEM 2011, JEOL), and atomic force microscope. The surface topography was analysed with a Bruker ICON AFM working in tapping mode in air. Raman spectra were obtained using an HR800 Jobin Yvon Horiba excited at 473 nm at room temperature. Surface chemistry was probed using X-ray Photoelectron Spectroscopy (XPS) using a ThermoFisher Scientific Nexsa spectrometer with a 400 μm spot size. The monochromatic X-ray source corresponds to the Al Kα line (λ = 1486.6 eV; pass energy (survey/HR): 200 eV/20 eV; dwell time: 100 ms; step size (survey/HR): 1 eV/0.1 eV). Quantification is performed on the basis of photopeak areas after Shirley-type background subtraction, using the ThermoFisher Scientific Avantage software and its 'ALTHERMO1' library. The mass of the samples was measured with a Mettler Toledo XPR205 balance.

Electrochemical characterization

The electrochemical performance of the as-prepared sample was characterized by employing a three-electrode cell (Fig. S1). The working electrode was a $ZnMn_2O_4$ thin film, with an estimated mass of 30 μg, deposited on a platinum substrate without any additives (no conductive carbon, no polymer binder), while zinc metal was used for the counter and reference electrodes. The electrolyte was a mixed solution of 1 M $ZnSO_4$ and 0.05 M $MnSO_4$ in distilled water. The cyclic voltammetry plot was acquired within the potential window of 0.8 V to 1.8 V (*vs.* Zn^{2+}/Zn), and the galvanostatic charge/discharge plots were obtained at room temperature using an Origalys Work Station (origaFlex-OGF ± 0.1A). From GCD the curves, the specific gravimetric capacity C_m, energy density E_m and power density P_m were calculated using eqn (1)–(3), where U is the voltage, I the discharging current, m the cathode material mass and t the discharging time.

$$C_m = \frac{I\Delta t}{m} \quad (1)$$

$$E_m = \frac{I\int U\mathrm{d}t}{m} \quad (2)$$

$$P_m = \frac{E_m}{t} \quad (3)$$

Results and discussion

Plasma $ZnMn_2O_4$ thin film formation, structure and microstructure

In order to highlight the role of plasma and substrate temperature on sample crystallinity and $ZnMn_2O_4$ formation, several thin films were deposited with different substrate temperatures in the presence of plasma or not (without plasma: 250 °C; with plasma: 50 °C, 145 °C, 175 °C and 200 °C). Fig. 2a shows the X-ray diffraction (XRD) patterns of the corresponding thin films. The diffractogram of the sample elaborated without plasma at 250 °C (Fig. 2a, red) shows only a very broad contribution at 2θ = 22°, which could be attributed to the amorphous quartz substrate. It seems that the thin film deposited under these conditions is amorphous. Diffractograms of the samples elaborated in the presence of plasma discharge with substrate temperatures from 50 °C to 200 °C (Fig. 2a, dark) have in common the characteristic diffraction peaks of pure spinel $ZnMn_2O_4$. These observations highlight the essential role of plasma discharge in directly obtaining, at temperatures below 200 °C, crystalline thin films of $ZnMn_2O_4$. From here, the sample elaborated without plasma will be named ZMO 250 and the samples elaborated with plasma will be named Plasma-ZMO 50, -ZMO 145, -ZMO 175 and -ZMO 200. In the presence of plasma discharge, when the substrate temperature increases from 50 °C to 200 °C, the peak width highly decreases. In fact, the very broad diffraction peaks observed in the Plasma-ZMO 50 and Plasma-ZMO 145 diffractograms suggest the presence of very small crystalline domains of just a few nanometers. At 175 °C and 200 °C, the nanoparticle size increases to 15–20 nm (size

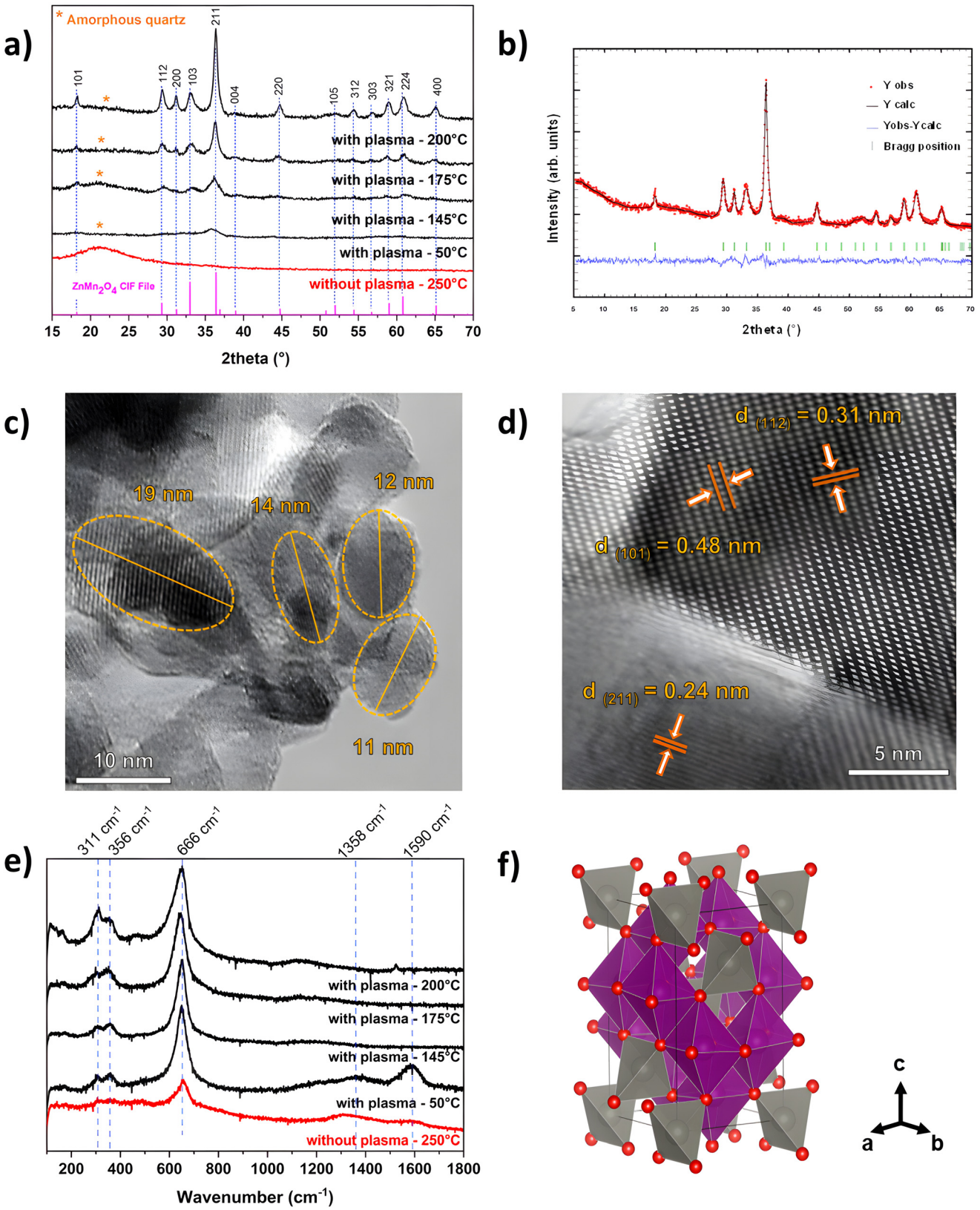

Fig. 2 a) DRX patterns of ZMO 250, and Plasma-ZMO 50, -ZMO 145, -ZMO 175 and -ZMO 200. b) Rietveld refined Plasma-ZMO 200 XRD pattern. c and d) HRTEM images of Plasma-ZMO 200. e) Raman spectra of ZMO 250, and Plasma-ZMO 50, -ZMO 145, -ZMO 175 and -ZMO 200. f) Crystallographic structure of $ZnMn_2O_4$.

estimated with Scherrer's equation using the (112) peak full width half maximum FWHM). Thus, the substrate temperature promotes the crystal growth and the nanoparticle size. In the Plasma-ZMO 200 diffractogram, an unexpected peak intensity ratio and non-constant peak width are observed, in particular for the 103 and 211 peaks. This suggests potential particular structural and microstructural characteristics compared to the isotropic $ZnMn_2O_4$ crystal (Fig. 2f). Based on this observation, Rietveld refinement was performed on the Plasma-ZMO 200 diffractogram implementing an anisotropic grain size model. The Rietveld refinement results are presented in Fig. 2b. Structural, microstructural and goodness of fit information are summarized in Table 1.

All peaks are well assigned to the I_{41}/amd space group (space group no. 141) and the structural parameters (unit cell, atom positions and occupancy) are consistent with the literature. The refinement data correspond to a negligible amount of microstrain. The particle size is thus considered to be the main contribution to the peak enlargement. The crystal domain sizes in the three directions show that the Plasma-ZMO 200 nanoparticles are anisotropic with a large shape factor, suggesting the potential formation of plate-shaped nanoparticles. The good quality of the refinement using the anisotropic grain size model suggests that the film is not textured. In order to confirm the particle size obtained with Rietveld refinement, the High Resolution Transmission Electronic Microscopy (HRTEM) images of Plasma-ZMO 200 are displayed in Fig. 2c and d. A clear lattice structure is observed. Crystalline domains of 14–19 nm can be observed with anisotropic shape. This justifies the anisotropic broadening model considerations. Inter-reticular distances of 0.483 nm, 0.305 nm and 0.244 nm are also calculated and matched, respectively, to the (101), (112) and (122) planes of the spinel $ZnMn_2O_4$.

The Raman spectra of samples elaborated with and without plasma are displayed in Fig. 2e. According to group theory, the factorial group analysis gives 10 Raman active modes. Indeed, $ZnMn_2O_4$ belongs to AMn_2O_4 spinels (A = Mn, Mg, and Zn), which have the following phonon modes T = $2A_{1g}$ + $3B_{1g}$ + B_{2g} + $4E_g$.[53] All Raman spectra of the ZMO thin layers show vibrational bands. Surprisingly, the ZMO 250 spectra exhibit one Raman vibrational mode at 665 cm^{-1}. It seems that heating at 250 °C leads to the formation of metal–oxygen bonds. The Plasma-ZMO 50, -ZMO 145, -ZMO 175 and -ZMO 200 spectra show three Raman vibrational modes at 311, 356 and 666 cm^{-1}, which can well match the $ZnMn_2O_4$ spinel phase. The low frequency modes (311 and 356 cm^{-1}) are the responses of the octahedral BO_6 sites; the high-frequency mode at 666 cm^{-1} can be ascribed to vibrations involving the motion of oxygens inside the tetrahedral unit AO_4, which can represent A_{1g} symmetry.[54,55] So, the formation of Mn–O and Zn–O bonds does not seem to be dependent on the substrate temperature. However, at low temperature (50 °C), two large bands are observed at 1358 cm^{-1} and 1590 cm^{-1}, which can be attributed to the G band and D band of amorphous carbon. This means that at low substrate temperature, there is residual carbon from the organometallic precursors. But at high temperatures, all of the precursor carbon is converted into CO and CO_2.

The surface of the ZMO 200 sample was characterized by X-ray Photoelectron Spectroscopy (XPS) in order to investigate the valence state of the Mn atoms and, consequently, to confirm the formation of the $ZnMn_2O_4$ spinel phase in thin films fabricated by the spray plasma process. The wide-scan XPS spectrum is shown in Fig. 3a. Peaks corresponding to Zn, Mn, O, and C elements are clearly observed. Fig. 3b displays the high-resolution XPS spectrum of the Mn 2p core level, where two distinct peaks centered at 641.0 eV and 653.1 eV correspond to Mn $2p_{3/2}$ and Mn $2p_{1/2}$, respectively. These two peaks are separated by a binding energy of ΔE = 12.1 eV, confirming the presence of Mn^{3+} species in spinel $ZnMn_2O_4$.[56–58] Fig. 3c presents the high-resolution XPS spectrum of the Zn 2p core level. The two peaks located at 1021.3 eV and 1044.4 eV correspond to Zn $2p_{3/2}$ and Zn $2p_{1/2}$ of Zn^{2+}, respectively. The energy separation between them, ΔE = 23.1 eV, is consistent with values reported in the literature.[58,59] The O 1s core-level spectrum, shown in Fig. 3d, exhibits a main contribution with a shoulder feature. After reconstruction, the component at 529.6 eV is attributed to oxygen atoms in the metal–oxide bonds (Mn–O and Zn–O).[60,61] The component at 531.6 eV may be assigned to –OH and C–O groups,[59] and/or to adsorbed oxidized species on the surface, such as water vapor.[61,62] Finally, Fig. 3e presents the XPS spectrum of the C 1s core level. Reconstruction of the spectrum reveals three components: the peak at 285.1 eV corresponds to C–C bonds (sp^3-hybridized carbon), the one at 286.3 eV is associated with C–O bonds, and the peak at 288.6 eV is attributed to O–C═O groups.[62] Given that the X-ray diagram and Raman spectrum of the ZMO 200 sample show no features related to carbon, these C 1s contributions are most likely due to surface contamination.

Table 1 Rietveld analysis of the Plasma-ZMO 200 thin film

Phase		$ZnMn_2O_4$			
Space group		I_{41}/amd			
System		*Tetragonal*			
Lattice					
a		5.74 Å			
c		9.18 Å			
Atomic positions					
Atom	*Wyckoff site*	*x*	*y*	*z*	*Occupancy*
Zn	*4(a)*	0	0.25	0.375	0.125
Mn	*8(d)*	0	0	0	0.25
O	*16(h)*	0	0.513	0.236	0.5
Crystalline size domains					
Orientation		(200)		(101)	(004)
Size		20.5 nm		14.9 nm	3.4 nm
Goodness of the fit					
χ^2			2.23		
R_p			3.61		
R_{wp}			4.58		
R_{exp}			3.07		

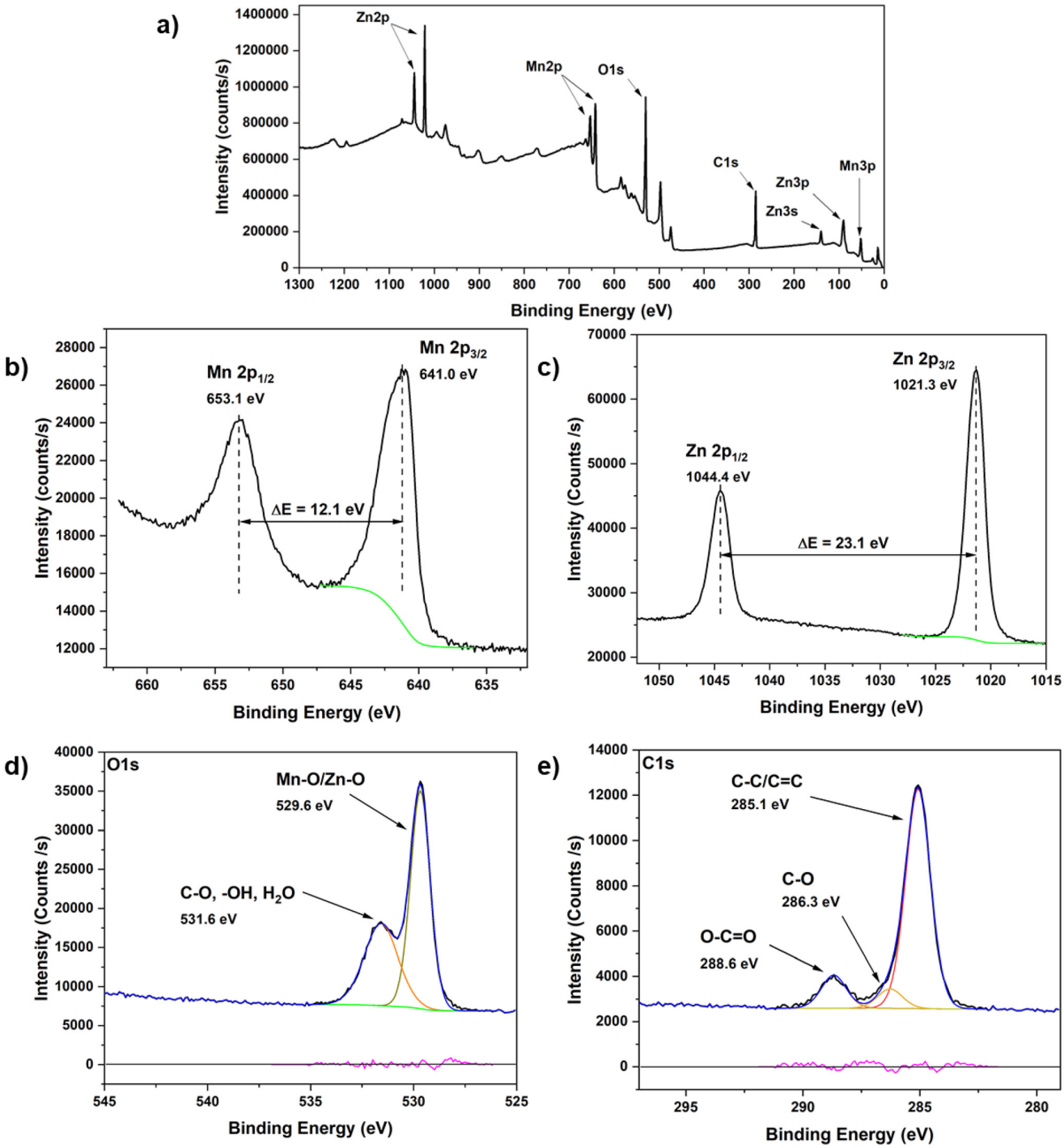

Fig. 3 a) Full XPS spectrum of ZMO 200. b) XPS spectra of Mn 2p. c) XPS spectra of Zn 2p. d) XPS spectra of O 1s. e) XPS spectra of C 1s.

In our experimental conditions the plasma is considered as a non-equilibrium medium where electrons acquire mean energy, to be in the range of 3–5 eV (measured by the Langmuir probe technique and Optical Emission Spectroscopy method).[63,64] The kinetic energy of electrons is sufficient to the break down bonds in chemicals (3.58 eV for the C–C bond). Moreover, in previous work, we demonstrated that in the range of plasma power applied, oxidant species, *e.g.* O and OH radicals, are formed and are able to oxidize the fragments of chemical precursor injected in the plasma participating in the formation of metal oxide thin films.[65,66] In our experimental conditions, the temperature of the reactor walls remains generally around 60–70 °C. In previous work, we estimated the temperature inside the plasma vicinity to be equal to (392 ± 50) K, independent of the RF power in the range explored in similar conditions as presented in this work, measuring the rotational temperature of the OH radical $(A^2\sum^+ - X^2\pi)(0,0)$ transition and from the

Boltzmann plot method of the OH emission lines.[48] It is noteworthy that the rotational temperature represents the thermal temperature of plasma gas rather than the electronic temperature. The fact that in conventional elaboration methods the oxidation of manganese acetate necessitates temperatures over 500 °C confirms that, in our conditions where the temperature doesn't exceed 70 °C, the chemical transformation of the starting materials into $ZnMn_2O_4$ is governed by electronic collisional processes *via* radical species.

Plasma $ZnMn_2O_4$ morphology

Scanning Electronic Microscopy (SEM) images at different scales of Plasma-ZMO 200 surface are shown in Fig. 4a and b. The substrate is entirely coated by the thin film and a heterogeneous and rough surface is observable. The Plasma-ZMO 200 morphology is similar to a cauliflower-like microstructure. Cauliflowers, of average size between 1 μm and 4 μm, are stuck together giving a high roughness appearance. Each micro-cauliflower is composed of spherical agglomerates of 400–600 nm, which are made of smaller particles and aggregates of 50–70 nm. In order to investigate the thin film thickness and growing mechanism, a straight cut of Plasma-ZMO 200 deposited on a Si substrate was performed. Fig. 4c shows a SEM image of the Plasma-ZMO 200 thickness. After only 30 min of deposition time, a thickness of 1.4 μm can be reached. Plasma-ZMO 200 seems to be a superposition of monolayers of 50–100 nm with distortions caused by spherical hollows. They could be the result of solvent evaporation during material deposition. The element mapping shown in Fig. 4d indicates that Zn, Mn and O are homogenously distributed in the whole film thickness. Each monolayer, thus, is composed of $ZnMn_2O_4$. The Atomic Force Microscopy (AFM) topography shown in Fig. 2e indicates that Plasma-ZMO 200 has a very rough surface. Indeed, its measured root mean square (RMS) roughness reaches 320.5 nm. This leads to a large surface area, which can increase massively the electrochemical performance of the Plasma-ZMO 200 cathode.

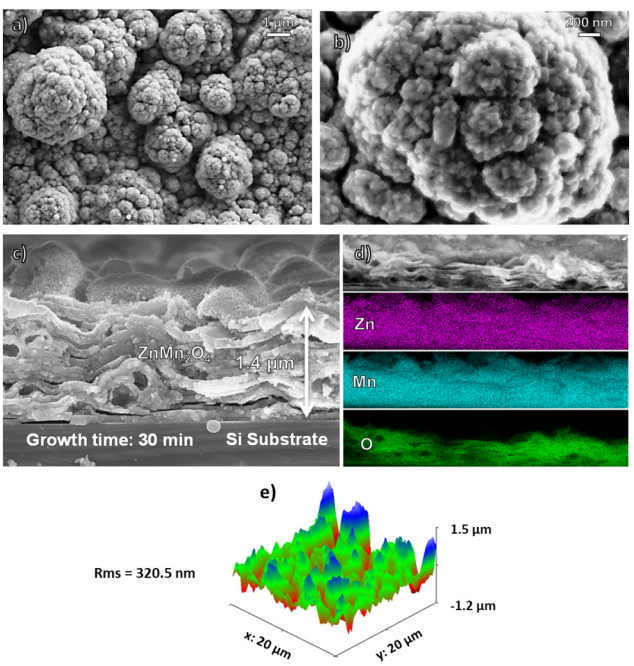

Fig. 4 a and b) SEM images of the Plasma-ZMO 200 surface. c) SEM image of a Plasma-ZMO 200 straight section. d) EDX elemental mapping images. e) AFM micrograph of Plasma-ZMO 200.

Plasma $ZnMn_2O_4$ as a ZIB cathode

To evaluate the electrochemical performance of Plasma-ZMO 200 as a ZIB cathode, a film was deposited on a platinum electrode. As indicated previously, no additives were added and annealing was not necessary to elaborate our films.

Fig. 5a and b show the cyclic voltammetry (CV) profiles of the Plasma-ZMO 200 cathode in the potential window of 0.8–1.8 V, recorded at scan rates of 1 mV s^{-1} (Fig. 5a) and 0.1 mV s^{-1} (Fig. 5b). At the higher scan rate, the CV curves display a single oxidation peak at 1.55 V during the anodic sweep and two reduction peaks at 1.19 V and 1.37 V during the cathodic sweep. At the lower scan rate, two distinct oxidation peaks at 1.53 V and 1.61 V emerge, while the two reduction peaks remain visible at 1.19 V and 1.37 V during the cathodic sweep. According to the literature, the interpretation of these current peaks remains controversial, as no consensus has been reached regarding the reaction mechanisms governing this class of batteries.[67] Although a large number of studies address MnO_2 cathodes, very few propose detailed reaction mechanisms for $ZnMn_2O_4$ cathodes. Nevertheless, two plausible mechanisms may be considered in the context of this work. The first involves Zn^{2+} intercalation and deintercalation. The oxidation peaks observed in the CV profiles of the Plasma-ZMO 200 cathode are attributed to the oxidation of Mn^{4+} atoms within the $ZnMn_2O_4$ spinel structure, induced by Zn^{2+} deintercalation. This process is ascribed to the strong electrostatic repulsion of neighbouring Mn cations occupying octahedral sites. The reduction peaks are instead associated with the reduction of Mn atoms in the spinel framework caused by Zn^{2+} intercalation. The presence of two oxidation and two reduction peaks is interpreted as stepwise Zn^{2+} deintercalation and intercalation, respectively.[28,59,68–70] The second mechanism considers the co-insertion and co-extraction of H^+ and Zn^{2+} ions. In fact, other reports suggest that the occurrence of two anodic and two cathodic peaks indicates that the system is governed by two distinct electrochemical processes, namely the reversible insertion of protons (H^+) and Zn^{2+} ions, which accompanies the Mn redox transitions in the $ZnMn_2O_4$ structure.[45,71,72] In this scenario, several authors have reported the precipitation of zinc hydroxysulfate ($Zn_4(OH)_6SO_4{\cdot}xH_2O$, commonly referred to as ZHS) on the cathode surface. Proton insertion into manganese oxides depletes H_3O^+ ions at the solid–liquid interface, leading to a local pH increase and subsequent ZHS deposition.[45]

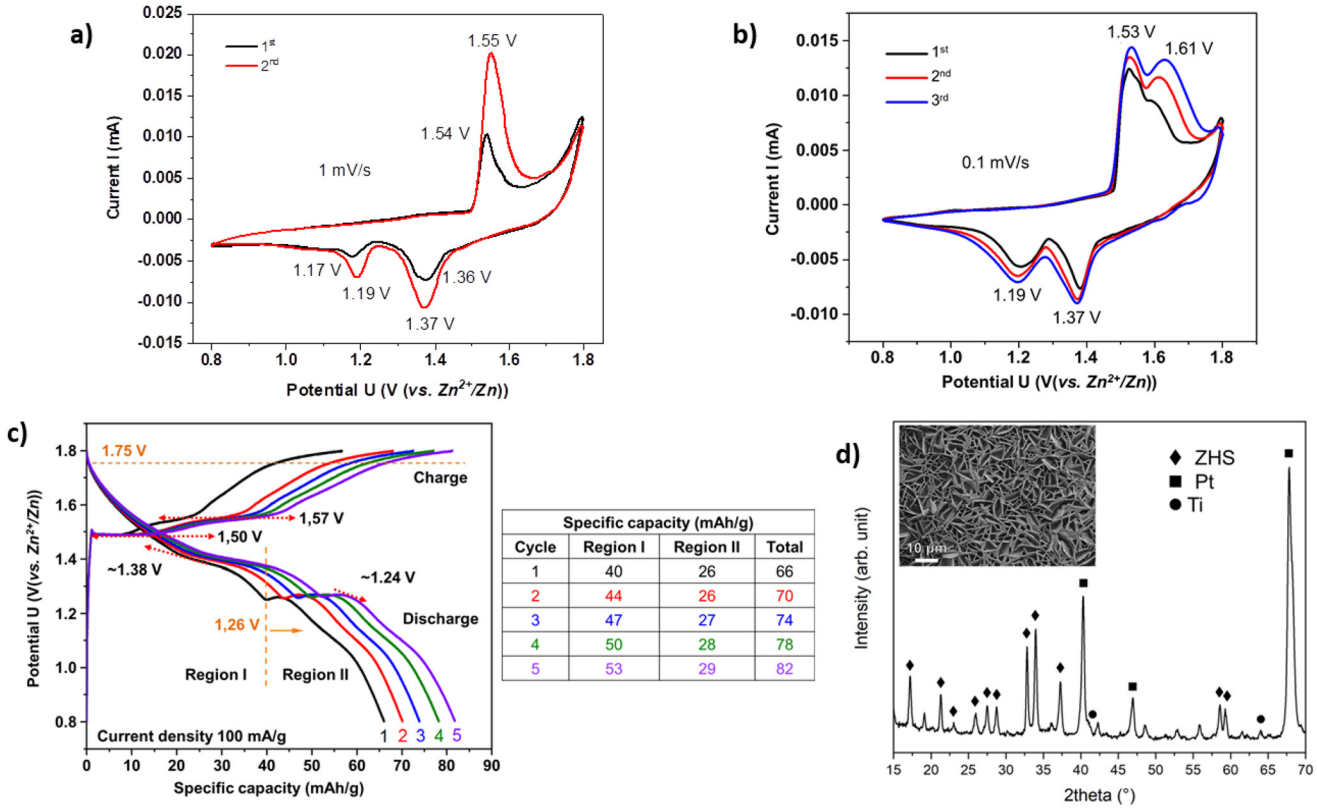

Specific capacity (mAh/g)			
Cycle	Region I	Region II	Total
1	40	26	66
2	44	26	70
3	47	27	74
4	50	28	78
5	53	29	82

Fig. 5 Plasma-ZMO 200 cathode electrochemical characterization. a) CV curves at a scan rate of 1 mV s^{-1}. b) CV curves at a scan rate of 0.1 mV s^{-1}. c) Galvanostatic charge/discharge curves at 100 mA g^{-1}. d) *Ex situ* X-ray diffraction pattern and scanning electronic micrograph (inset) of the cathode surface after the 5th discharge.

Meanwhile, the increase of redox peak current during the first CV scans indicates the possible existence of an activation process or a better accessibility to the whole material.

To track the evolution of the specific capacity as a function of cycling, the galvanostatic charge/discharge profiles at 100 mA g^{-1} between 0.8–1.8 V are superimposed in Fig. 5c. In the charge profiles, two distinct oxidation plateaus can be observed at 1.50 V and 1.57 V, while two reduction pseudo-plateaus appear at approximately 1.24 V and 1.38 V in the discharge profiles. The positions of these plateaus and pseudo-plateaus are relatively close to the oxidation and reduction peak potentials observed in the CV profiles and are in good agreement with values reported in the literature.[24,26,28,59,68,72,73] The discharge plateaus are separated by an inflection point—often referred to as a voltage tip—located at 1.26 V, which is commonly observed for manganese-based cathodes in $ZnSO_4$ electrolytes. This voltage tip has been interpreted either as the nucleation point of ZHS[45] or as the onset of a decrease in the Zn^{2+} diffusion coefficient according to another report.[74] Based on this interpretation, the galvanostatic discharge profile of the Plasma-ZMO 200 cathode can thus be divided into two distinct regions: region I, prior to the 1.26 V tip, and region II, after the 1.26 V tip. The overall capacity increases progressively with cycling, as shown in the table of Fig. 5c. The first cycle delivers only 56 mA h g^{-1} during charge and 66 mA h g^{-1} during discharge. In the second cycle, the discharge capacity rises to 70 mA h g^{-1}, corresponding to a 6% capacity gain, and continues to increase until it reaches 82 mA h g^{-1} by the fifth cycle, representing a 24% gain relative to the first cycle. This capacity enhancement corroborates the observations made from the CV profiles of the Plasma-ZMO 200 cathode. A closer examination of regions I and II reveals that the capacity contribution of region I is consistently greater than that of region II, regardless of the cycle number, and that the contribution of region I increases more rapidly than that of region II (see table in Fig. 5c). These observations clearly indicate that the two regions are associated with distinct electrochemical kinetics. According to the literature, region I is attributed to the capacity arising from the H^+ insertion step, whereas region II corresponds to the capacity associated with Zn^{2+} intercalation.[24]

After the galvanostatic charge/discharge measurements, at the end of the 5th discharge, the Plasma-ZMO 200 cathode sample was characterized by scanning electron microscopy (SEM) and X-ray diffraction (XRD), and the results are shown in Fig. 5d. The XRD pattern reveals the presence of diffraction peaks characteristic of the $Zn_4(OH)_6SO_4{\cdot}4H_2O$ phase, while the SEM images of the Plasma-ZMO 200 cathode sample surface at the end of the discharge show lamellar structures that are completely different from the morphology

observed before the charge/discharge cycling. According to the literature,[72] such structures are characteristic of ZHS deposits forming on manganese oxide cathode surfaces after the 1.26 V voltage tip during discharge. Consequently, it can be concluded that ZHS deposits form on the surface of the Plasma-ZMO 200 cathode sample during discharge and that this process contributes to the recorded electrochemical signal. Given that the reaction mechanism in this type of system remains complex, the results presented above do not allow for a clear identification of all the chemical processes responsible for the observed electrochemical signal. Nevertheless, by combining these results with conclusions drawn from the literature, a mechanism involving the co-insertion of H^+ and Zn^{2+}, accompanied by the electrodeposition/dissolution of ZHS, appears plausible to explain the electrochemical behaviour of the Plasma-ZMO 200 cathode.

In order to investigate the behaviour of the Plasma-ZMO 200 cathode under a high number of cycles and at a high current density, the sample was cycled at 1 A g^{-1} for 1100 cycles. Fig. 6a shows the evolution of the charge and discharge capacities as well as the coulombic efficiency during this cycling, while Fig. 6b presents the charge/discharge profiles of the 1st, 100th, 200th, 500th, 800th, 900th, 1000th and 1100th cycle. Both the charge and discharge specific capacities increase over the 1100 cycles at 1 A g^{-1}, thus confirming the observations made from the CV profiles in Fig. 5a and b and the galvanostatic charge/discharge measurements at 100 mA g^{-1}. The initial discharge capacity is only 20 mA h g^{-1}. It remains stable for about fifty cycles but, surprisingly, begins to increase, reaching 155 mA h g^{-1} after 1100 cycles. The first cycle shows a coulombic efficiency of 62%. This shows an initial irreversible process, which could be due to SEI formation, irreversible ion trapping and/or side

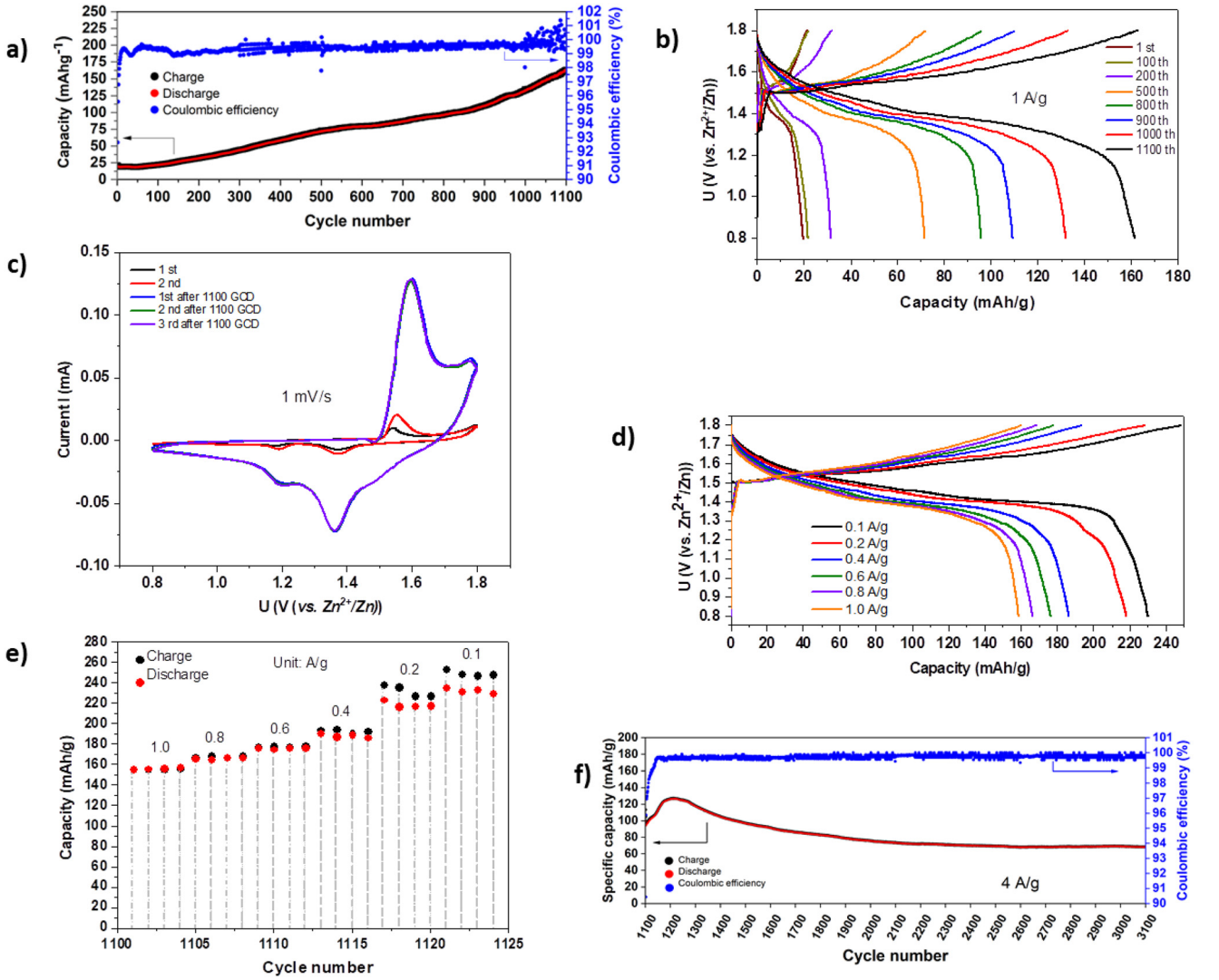

Fig. 6 Plasma-ZMO 200 cathode electrochemical performances. a) Capacity evolution over 1100 cycles at 1 A g^{-1}. b) Galvanostatic charge/discharge curves at 1 A g^{-1}. c) CV curves before and after the activation phase at 1 mV s^{-1}. d) Galvanostatic charge/discharge curves at different current densities. e) Rate performance at different current densities. f) Capacity evolution over 2000 cycles at 4 A g^{-1}.

reactions. From the second cycle onward, the CE increases rapidly, and after 20 cycles it reaches between 98% and 99%. The subsequent cycles typically show much higher efficiencies than the initial ones indicating that the system has reached a more reversible electrochemical regime.

Analysis of the profiles in Fig. 6b indicates that the capacity increase is associated with the elongation of the 1.50 V plateau (charge) and the pseudo-plateau around 1.38 V (discharge). CV plots of Plasma-ZMO 200 after 1100 cycles (Fig. 6c) also confirms the GCD results as the redox peak current increases significantly. This capacity growth over prolonged cycling could be due to reversible ZHS deposition/dissolution according to the rising capacity from the H^+ insertion step as observed in Fig. 5c. In fact, in the GCD curves shown in Fig. 6b, we can observe the disappearance of the 1.26 V tip. This means that at high current density, the insertion of H^+ responsible of ZHS formation is the main electrochemical phenomenon responsible for the specific capacity. Furthermore, according to S. Li *et al.*, the ZHS layer formed on the cathode surface may act as a passivation layer, enhancing the cycling stability of the cathode.[47] Zhao *et al.* even reported a discharge specific capacity of approximately 123 mA h g^{-1} using a cathode composed solely of ZHS.[75]

The rate performance of the Plasma-ZMO 200 cathode after the 1100th cycle, shown in Fig. 6d and e, was investigated at different current densities from 1 A g^{-1} to 0.1 A g^{-1}. The discharge capacity increases when the current density decreases. At current densities of 0.8, 0.6, 0.4, 0.2, and 0.1 A g^{-1}, the reversible discharge capacities are 166, 176, 190, 223 and 235 mA h g^{-1}, respectively. The energy density and power density of the Plasma-ZMO 200 cathode at a discharging current density of 0.1 A g^{-1} are 331 W h kg^{-1} and 86 W kg^{-1} using eqn (2) and (3). A second cycling stage was performed on the Plasma-ZMO 200 sample by further increasing the current density to 4 A g^{-1} over 2000 cycles (3100 GCD cycles in total). Fig. 6f shows the evolution of the specific capacity and coulombic efficiency of Plasma-ZMO 200 during this second stability test. After a first capacity increase stage to 126 mA h g^{-1} at 100 cycles, the specific capacity drops to a constant value of 68 mA h g^{-1}. At this very high current density, the phenomena leading to an increase in the specific capacity do not occur. It can therefore be suggested that the kinetics of these reactions are relatively slow. The capacity drop could also be explained by the structural degradation of the cathode, or simply by the loss of mass due to the delamination of part of the active material from the current collector, given that the cycling period here was approximately two months.

Finally, a brief comparison of the electrochemical performance of the ZMO 200 thin film elaborated by plasma with that of ZMO-type cathodes prepared with conventional synthesis methods is presented in Table 2. The performance of ZMO 200 is fully comparable to that of its counterparts, while maintaining the distinctive advantage of being free from carbon and binder additives. It is acknowledged that this comparison does not take into account the influence of cathode thickness and its consequent effect on electron diffusion between the surface and the current collector. Nevertheless, the table provides a useful overview of the recent progress achieved in ZMO-based cathodes for zinc-ion batteries and outlines prospective performance targets for future developments.

Conclusion

In this work, we report for the first time the one-step fabrication of nanostructured $ZnMn_2O_4$ thin films by a plasma-based technique. Remarkably, the as-deposited layers were already crystallized without any post-annealing, and at a substrate temperature of 200 °C, with an average crystallite of 14 nm. The films exhibited a rough, cauliflower-like morphology. The plasma process allows the deposition of thin films with a thickness of 1.4 μm in only 30 min. The as-prepared $ZnMn_2O_4$ electrodes (without conductive carbon or polymer binder) delivered a discharge capacity of 235 mA h g^{-1} at 0.1 A g^{-1} in zinc-ion batteries. A pronounced activation process was observed, with the reversible capacity increasing

Table 2 Comparative table of the electrochemical performances of selected ZIB cathodes fabricated by conventional methods and the ZMO 200 thin film produced *via* plasma spray

Cathode	Elaboration method	Electrolyte	Maximum specific capacity	Cyclability	Ref.
Oxygen-deficient Mn_3O_4	Solvothermal	2 M $ZnSO_4$ + 0.2 M $MnSO_4$	386 mA h g^{-1} at 0.1 A g^{-1}	272% after 500 cycles at 0.5 A g^{-1}	76
α-MnO_2 nano-wire/CNT	Hydrothermal	2 M $ZnSO_4$	330 mA h g^{-1} at 0.05 A g^{-1}	8% over 2500 cycle at 3 A g^{-1}	77
$VO_2{\cdot}xH_2O$ nanoribbons	Hydrothermal	3 M $Zn(CF_3SO_3)_2$	235.63 mA h g^{-1} at 0.1 A g^{-1}	82% after 1000 cycles at 1 A g^{-1}	78
$ZnMn_2O_4/Mn_2O_3$	Surfactant-assisted solvothermal method	1 M $ZnSO_4$	152 mA h g^{-1} at 0.1 A g^{-1}	143% after 300 cycles at 0.5 A g^{-1}	70
Mn_2O_3@$ZnMn_2O_4$/C hollow micro-spheres	Hydrothermal	2 M $ZnSO_4$ + 0.1 M $MnSO_4$	289.9 mA h g^{-1} at 200 mA g^{-1}	203.5 mA h g^{-1} after cycling for 700 times at 1000 mA g^{-1}	79
MoS_2@N-CQDs	Solvothermal	3 M $Zn(OTf)_2$	258 mA h g^{-1} at 0.1 A g^{-1}	94.5% after 2000 cycles	80
$ZnMn_2O_4$	Spray plasma	1 M $ZnSO_4$ + 0.05 M $MnSO_4$	235 mA h g^{-1} at 0.1 A g^{-1}	70% after 2000 cycles at 4 A g^{-1}	This work

over 1100 cycles at 1 A g^{-1}, attributed to the formation of a ZHS phase at the cathode surface. Even at a high current density of 4 A g^{-1}, the electrodes retained about 70% of their capacity over 2000 cycles. These results highlight the potential of plasma processing as an environmentally friendly, low-cost route for producing high-performance electrode materials.

Author contributions

Mehrdad Nikravech conceived the project and provided the funding. Alex Lemarchand, Hubert Perrot and Mehrdad Nikravech supervised the work; Lounis H. Bekkar performed the experiments and the data analysis; Cyrille Bazin and Alex Lemarchand contributed to the X-ray diffraction analysis; Mathieu Frégnaux contributed to XPS analysis; Hubert Perrot contributed to the design, operation and discussion of the electrochemical analysis. Noël Girodon-Boulandet was involved in the design and realisation of the components needed for the plasma reactor running; Lounis H. Bekkar prepared the initial manuscript; Lounis H. Bekkar, Alex Lemarchand, Cyrille Bazin, Hubert Perrot and Mehrdad Nikravech contributed to the discussion and manuscript preparation/editing. All authors have given approval to the final version of the manuscript.

Conflicts of interest

There are no conflicts to declare.

Data availability

The data that support the findings of this study have been directly included in the main text. Additional raw data are available from the corresponding author (mehrdad.nikravech@lspm.cnrs.fr) upon reasonable request.

Supplementary information (SI): the SI file provides an additional comparative table of the electrochemical performances of selected ZMO cathodes fabricated by conventional methods, compared with the cathode material performance obtained in this work (ZMO 200 thin film produced *via* plasma spray). It also includes additional data related to electrochemical experiments, including sample preparation and cell measurement conditions. See DOI: https://doi.org/10.1039/d5lf00303b.

Acknowledgements

The authors acknowledge financial support from the federative research structure NAP Mosaic from Université Sorbonne Paris Nord. They also thank Maria Konstantakopoulou from Laboratoire des Sciences des Procédés et des Matériaux for the Transmission Electronic Microscopy analysis.

Notes and references

1 A. Kalair, N. Abas, M. S. Saleem, A. R. Kalair and N. Khan, *Energy Storage*, 2021, **3**, e135.
2 M. A. Hannan, S. B. Wali, P. J. Ker, M. S. A. Rahman, M. Mansor, V. K. Ramachandaramurthy, K. M. Muttaqi, T. M. I. Mahlia and Z. Y. Dong, *J. Energy Storage*, 2021, **42**, 103023.
3 https://eur-lex.europa.eu/legal-content/EN/TXT/HTML/?uri=CELEX:52019DC0176, (Accessed October 29, 2024).
4 Energy storage, https://www.iea.org/energy-system/electricity/grid-scale-storage, (accessed October 29, 2024).
5 G. Zubi, R. Dufo-López, M. Carvalho and G. Pasaoglu, *Renewable Sustainable Energy Rev.*, 2018, **89**, 292–308.
6 A. Manthiram, *ACS Cent. Sci.*, 2017, **3**, 1063–1069.
7 Q. Wang, B. Mao, S. I. Stoliarov and J. Sun, *Prog. Energy Combust. Sci.*, 2019, **73**, 95–131.
8 Commodities at a Glance: Special issue on strategic battery raw materials, 2020.
9 J.-Y. Hwang, S.-T. Myung and Y.-K. Sun, *Chem. Soc. Rev.*, 2017, **46**, 3529–3614.
10 R. Rajagopalan, Y. Tang, X. Ji, C. Jia and H. Wang, *Adv. Funct. Mater.*, 2020, **30**, 1909486.
11 M. M. Huie, D. C. Bock, E. S. Takeuchi, A. C. Marschilok and K. J. Takeuchi, *Coord. Chem. Rev.*, 2015, **287**, 15–27.
12 J. Ming, J. Guo, C. Xia, W. Wang and H. N. Alshareef, *Mater. Sci. Eng., R*, 2019, **135**, 58–84.
13 R. J. Gummow, G. Vamvounis, M. B. Kannan and Y. He, *Adv. Mater.*, 2018, **30**, 1801702.
14 Y. Zhang, S. Liu, Y. Ji, J. Ma and H. Yu, *Adv. Mater.*, 2018, **30**, 1706310.
15 X. Zeng, J. Hao, Z. Wang, J. Mao and Z. Guo, *Energy Storage Mater.*, 2019, **20**, 410–437.
16 H. Li, L. Ma, C. Han, Z. Wang, Z. Liu, Z. Tang and C. Zhi, *Nano Energy*, 2019, **62**, 550–587.
17 W. Xu and Y. Wang, *Nano-Micro Lett.*, 2019, **11**, 90.
18 X. Jia, C. Liu, Z. G. Neale, J. Yang and G. Cao, *Chem. Rev.*, 2020, **120**, 7795–7866.
19 Y. Zhao, Y. Zhu and X. Zhang, *InfoMat*, 2020, **2**, 237–260.
20 Y. Zhang, A. Chen and J. Sun, *J. Energy Chem.*, 2021, **54**, 655–667.
21 G. Zampardi and F. La Mantia, *Curr. Opin. Electrochem.*, 2020, **21**, 84–92.
22 W. Shi, W. S. V. Lee and J. Xue, *ChemSusChem*, 2021, **14**, 1634–1658.
23 M. H. Alfaruqi, V. Mathew, J. Gim, S. Kim, J. Song, J. P. Baboo, S. H. Choi and J. Kim, *Chem. Mater.*, 2015, **27**, 3609–3620.
24 H. Zhang, J. Wang, Q. Liu, W. He, Z. Lai, X. Zhang, M. Yu, Y. Tong and X. Lu, *Energy Storage Mater.*, 2019, **21**, 154–161.
25 Z. Iskandar Radzi, K. Helmy Arifin, M. Zieauddin Kufian, V. Balakrishnan, S. Rohani Sheikh Raihan, N. Abd Rahim and R. Subramaniam, *J. Electroanal. Chem.*, 2022, **920**, 116623.
26 X. Wu, Y. Xiang, Q. Peng, X. Wu, Y. Li, F. Tang, R. Song, Z. Liu, Z. He and X. Wu, *J. Mater. Chem. A*, 2017, **5**, 17990–17997.
27 L. Yan, X. Zeng, Z. Li, X. Meng, D. Wei, T. Liu, M. Ling, Z. Lin and C. Liang, *Mater. Today Energy*, 2019, **13**, 323–330.
28 F. Gao, B. Mei, X. Xu, J. Ren, D. Zhao, Z. Zhang, Z. Wang, Y. Wu, X. Liu and Y. Zhang, *Chem. Eng. J.*, 2022, **448**, 137742.
29 C. Yang, M. Han, H. Yan, F. Li, M. Shi and L. Zhao, *J. Power Sources*, 2020, **452**, 227826.

30 K. Cai, S. Luo, J. Feng, J. Wang, Y. Zhan, Q. Wang, Y. Zhang and X. Liu, *Chem. Rec.*, 2022, **22**, e202100169.
31 N. Zhang, F. Cheng, Y. Liu, Q. Zhao, K. Lei, C. Chen, X. Liu and J. Chen, *J. Am. Chem. Soc.*, 2016, **138**, 12894–12901.
32 P. Kommu, G. P. Singh and A. S. Bhattacharyya, *J. Energy Storage*, 2018, **16**, 156–159.
33 R. Gherbi, Y. Bessekhouad and M. Trari, *J. Phys. Chem. Solids*, 2016, **89**, 69–77.
34 M. S. Song, Y. J. Cho, D. Y. Yoon, S. Nahm, S. H. Oh, K. Woo, J. M. Ko and W. I. Cho, *Electrochim. Acta*, 2014, **137**, 266–272.
35 L. Xiao, Y. Yang, J. Yin, Q. Li and L. Zhang, *J. Power Sources*, 2009, **194**, 1089–1093.
36 S. Vinoth, M. Govindasamy, S.-F. Wang, A. A. Alothman and R. A. Alshgari, *Microchim. Acta*, 2021, **188**, 131.
37 T. Ni, Y. Zhong, J. Sunarso, W. Zhou, R. Cai and Z. Shao, *Electrochim. Acta*, 2016, **207**, 58–65.
38 S. Cheng, Q. Ru, Y. Gao, M. Zhen, F. Chen, L. Wei and F. C.-C. Ling, *Chem. Eng. J.*, 2021, **406**, 126133.
39 Q. Fang, C. Chen, Z. Yang, X. Chen, X. Chen and T. Liu, *J. Alloys Compd.*, 2020, **826**, 154084.
40 G. Zhang, L. Yu, H. B. Wu, H. E. Hoster and X. W. Lou, *Adv. Mater.*, 2012, **24**, 4609–4613.
41 T. Feng, J. Yang, S. Dai, J. Wang and M. Wu, *Trans. Nonferrous Met. Soc. China*, 2021, **31**, 265–276.
42 S.-W. Kim, H.-W. Lee, P. Muralidharan, D.-H. Seo, W.-S. Yoon, D. K. Kim and K. Kang, *Nano Res.*, 2011, **4**, 505–510.
43 J. P. Morán-Lázaro, E. S. Guillen-López, F. López-Urias, E. Muñoz-Sandoval, O. Blanco-Alonso, H. Guillén-Bonilla, A. Guillén-Bonilla, V. M. Rodríguez-Betancourtt, M. Sanchez-Tizapa and M. D. la L. Olvera-Amador, *Sensors*, 2018, **18**, 701.
44 Z. Zheng, Y. Cheng, X. Yan, R. Wang and P. Zhang, *J. Mater. Chem. A*, 2013, **2**, 149–154.
45 S. Deng, Z. Tie, F. Yue, H. Cao, M. Yao and Z. Niu, *Angew. Chem., Int. Ed.*, 2022, **61**, e202115877.
46 Y. Huang, J. Mou, W. Liu, X. Wang, L. Dong, F. Kang and C. Xu, *Nano-Micro Lett.*, 2019, **11**, 49.
47 S. Li, D. Yu, L. Liu, S. Yao, X. Wang, X. Jin, D. Zhang and F. Du, *Chem. Eng. J.*, 2022, **430**, 132673.
48 K. Baba, C. Lazzaroni and M. Nikravech, *Plasma Chem. Plasma Process.*, 2014, **34**, 1433–1446.
49 H. M. Rietveld, *J. Appl. Crystallogr.*, 1969, **2**, 65–71.
50 *The Rietveld Method*, ed. R. A. Young, Oxford University Press, 1993.
51 J. Rodríguez-Carvajal, *Phys. B*, 1993, **192**, 55–69.
52 N. C. Popa, *J. Appl. Crystallogr.*, 1998, **31**, 176–180.
53 L. Malavasi, P. Galinetto, M. C. Mozzati, C. B. Azzoni and G. Flor, *Phys. Chem. Chem. Phys.*, 2002, **4**, 3876–3880.
54 K. Samanta, S. Dussan, R. S. Katiyar and P. Bhattacharya, *Appl. Phys. Lett.*, 2007, **90**, 261903.
55 H. Li, B. Song, W. J. Wang and X. L. Chen, *Mater. Chem. Phys.*, 2011, **130**, 39–44.
56 C. Yuan, L. Zhang, S. Zhu, H. Cao, J. Lin and L. Hou, *Nanotechnology*, 2015, **26**, 145401.
57 P. E. Saranya and S. Selladurai, *J. Mater. Sci.: Mater. Electron.*, 2018, **29**, 3326–3339.
58 J. G. Kim, S. H. Lee, Y. Kim and W. B. Kim, *ACS Appl. Mater. Interfaces*, 2013, **5**, 11321–11328.
59 L. Chen, Z. Yang, H. Qin, X. Zeng, J. Meng and H. Chen, *Electrochim. Acta*, 2019, **317**, 155–163.
60 P. Zhang, X. Li, Q. Zhao and S. Liu, *Nanoscale Res. Lett.*, 2011, **6**, 323.
61 X. Chen, Y. Zhang, H. Lin, P. Xia, X. Cai, X. Li, X. Li and W. Li, *J. Power Sources*, 2016, **312**, 137–145.
62 C. Shamitha, T. Senthil, L. Wu, B. S. Kumar and S. Anandhan, *J. Mater. Sci.: Mater. Electron.*, 2017, **28**, 15846–15860.
63 K. Baba, Développement et optimisation du procédé Spray Plasma de dépôt de couches minces d'oxyde de zinc : application aux cellules photovoltaïques, *Ph.D. thesis*, Université Paris 13, 2013.
64 I. Gafarov, G. Paskalov, C. Lazzaroni, M. Nikravech, K. Baba and V. Zheltukhin, Investigation of RF discharge parameters in diffusion regimes, 2017.
65 M. Nikravech, K. Baba, B. Leneindre and F. Rousseau, *Chem. Pap.*, 2012, **66**, 502–510.
66 C. Lazzaroni, K. Baba, M. Nikravech and P. Chabert, *J. Phys. D: Appl. Phys.*, 2012, **45**, 485207.
67 D. Chen, M. Lu, D. Cai, H. Yang and W. Han, *J. Energy Chem.*, 2021, **54**, 712–726.
68 L. Chen, Z. Yang, H. Qin, X. Zeng and J. Meng, *J. Power Sources*, 2019, **425**, 162–169.
69 S. Wang, S. Zhang, X. Chen, G. Yuan, B. Wang, J. Bai, H. Wang and G. Wang, *J. Colloid Interface Sci.*, 2020, **580**, 528–539.
70 S. Yang, M. Zhang, X. Wu, X. Wu, F. Zeng, Y. Li, S. Duan, D. Fan, Y. Yang and X. Wu, *J. Electroanal. Chem.*, 2019, **832**, 69–74.
71 W. Qiu, H. Xiao, H. Feng, Z. Lin, H. Gao, W. He and X. Lu, *Chem. Eng. J.*, 2021, **422**, 129890.
72 C. Huang, Q. Wang, D. Zhang and G. Shen, *Nano Res.*, 2022, **15**, 8118–8127.
73 S. Islam, M. H. Alfaruqi, D. Y. Putro, S. Park, S. Kim, S. Lee, M. S. Ahmed, V. Mathew, Y.-K. Sun, J.-Y. Hwang and J. Kim, *Adv. Sci.*, 2021, **8**, 2002636.
74 B. Wu, G. Zhang, M. Yan, T. Xiong, P. He, L. He, X. Xu and L. Mai, *Small*, 2018, **14**, 1703850.
75 S. Zhao, B. Han, D. Zhang, Q. Huang, L. Xiao, L. Chen, D. G. Ivey, Y. Deng and W. Wei, *J. Mater. Chem. A*, 2018, **6**, 5733–5739.
76 L. Jiang, Z. Wu, Y. Wang, W. Tian, Z. Yi, C. Cai, Y. Jiang and L. Hu, *ACS Nano*, 2019, **13**, 10376–10385.
77 F. Xiankai, X. Kaixiong, Z. Wei, D. Weina, Z. Hai, C. Liang and C. Han, *Carbon Energy*, 2024, **6**, e536.
78 G. Mahendra, R. Roy and A. K. Singh, *J. Power Sources*, 2024, **624**, 235515.
79 Z. Gao, G. Lu, L. Cao, Z. Zhu, Y. Li, F. Wei, Z. Ji, Y. Sui, J. Qi, Q. Meng and Y. Ren, *Dalton Trans.*, 2023, **52**, 1768–1776.
80 M. Hariram, P. K. Pal, A. S. Chandran, M. R. Nair, M. Kumar, M. K. Ganesha, A. K. Singh, B. Dasgupta, S. Goel, T. Roy, P. W. Menezes and D. Sarkar, *Small*, 2025, **21**, 2410408.